Communications Physics

https://doi.org/10.1038/s42005-026-02595-7

Article in Press

Magneto-optical observation of electrically generated orbital polarization in pristine Cu and oxidized Cu

Received: 13 July 2025

Accepted: 10 March 2026

Cite this article as: Ko, K.-H., Jo, D., Oppeneer, P.M. *et al.* Magneto-optical observation of electrically generated orbital polarization in pristine Cu and oxidized Cu. *Commun Phys* (2026). https://doi.org/10.1038/s42005-026-02595-7

Kyung-Hun Ko, Daegeun Jo, Peter M. Oppeneer, Hyun-Woo Lee & Gyung-Min Choi

Magneto-optical observation of electrically generated orbital polarization in pristine Cu and oxidized Cu

Kyung-Hun Ko[1†], Daegeun Jo[2,3†], Peter M. Oppeneer[2,3], Hyun-Woo Lee[4,5★] and Gyung-Min Choi[1★]

[1]Department of Energy Science, Sungkyunkwan University, Suwon 16419, Korea
[2]Department of Physics and Astronomy, Uppsala University, P.O. Box 516, SE-75120 Uppsala, Sweden
[3]Wallenberg Initiative Materials Science for Sustainability, Uppsala University, SE-75120 Uppsala, Sweden
[4]Department of Physics, Pohang University of Science and Technology, Pohang 37673, Korea
[5]Asia Pacific Center for Theoretical Physics, 77 Cheongam-ro, Pohang 37673, Korea
[†]These authors contributed equally.

[★]Correspondence to: hwl@postech.ac.kr (H.-W. Lee), gmchoi@skku.edu (G.-M. Choi)

Abstract

The electrical generation of orbital angular momentum in materials has attracted significant attention due to its fundamental importance and technological potential. Notably, recent experiments on orbital torque and terahertz emission suggest that Cu enables substantial charge-to-orbital interconversion upon oxidation. However, direct evidence of orbital generation in Cu remains elusive. In this work, we demonstrate current-induced orbital accumulation in pristine and naturally oxidized Cu films using magneto-optical Kerr effect measurements. We observe distinct thickness dependences of the Kerr signals in pristine and oxidized films, revealing bulk- and interface-driven orbital generation mechanisms corresponding to the orbital Hall effect and orbital Rashba-Edelstein effect, respectively. The extracted orbital diffusion length in Cu is significantly shorter than its known spin diffusion length, yet still exceeds atomic scales. These findings provide clear evidence of orbital generation in Cu and highlight the distinct bulk and interfacial mechanisms underlying it.

Introduction

Recent studies have theoretically suggested and experimentally demonstrated that the orbital angular momentum (OAM) of electrons can be generated and transported under an external electric bias.[1-3] Two main mechanisms are responsible for the electrical generation of OAM. In centrosymmetric systems, the orbital Hall effect (OHE)[4-7] generates a transverse orbital current (OAM current to be precise), which originates from the orbital texture of materials (Fig. 1a). Although, the orbital current itself is usually not directly observable, it leads to the accumulation of OAM at the sample edges. In systems with broken inversion symmetry, the orbital Rashba-Edelstein effect (OREE)[8] locally induces an OAM density (Fig. 1b). This electrically generated OAM can be utilized to manipulate the magnetization of a ferromagnet (FM) through orbital torque.[9] Notably, earlier experiments reported remarkably large torques in oxidized Cu/FM or oxidized Cu/heavy metal/FM structures.[10-19] These studies suggested that the OREE is strongly induced in oxidized Cu,[20] positioning Cu as a promising material for orbitronic device applications without relying on heavy elements.

However, conclusive evidence for OAM generation in oxidized Cu, as well as a clear understanding of its microscopic origin, remains elusive. The torque measurements with magnetic heterostructures face inherent challenges due to the existence of the FM layer and additional interfaces, rendering the interpretation of orbital torque in some previous experiments still controversial.[21] As a result, the orbital torque measurements alone do not offer definitive proof of the OREE in oxidized Cu. Similarly, in the THz emission experiment using the FM/Cu/MgO structure,[22] the observed electrical signal was attributed to the inverse OREE at the Cu/MgO interface. However, this measurement also resorts to the FM layer, and thus suffers from the same limitations as torque measurements. On the contrary, the magneto-optical Kerr effect (MOKE) measurement can detect OAM accumulation in a single layer without a FM layer. The detection sensitivity is determined by the magneto-optic constant (Q), and the Q value for orbital contribution can be much larger than that for spin contribution in a weak spin-orbit coupling system. Therefore, the MOKE experiment serves as a powerful tool for exploring the OAM generation in Cu.

Two fundamental issues should be addressed to verify the OAM generation in Cu. First, even in a single Cu layer, both bulk-originated (OHE) and interface-originated (OREE) mechanisms

can coexist. While it has been predicted that the former is generally negligible and the latter becomes significant upon oxidation, these speculations have not been firmly confirmed. Second, the symmetries of the OHE and OREE are identical to their spin counterparts, the spin Hall effect and the spin Rashba-Edelstein effect. This similarity makes it difficult to distinguish whether an experimental signal arises from orbital[13,15,20] or spin[11] contributions. In fact, recent theoretical studies[23-25] reported that theoretically predicted orbital relaxation lengths in several transition metals are significantly shorter than experimentally reported values,[26-29] which led to the speculation[23] that experimentally evaluated orbital relaxation lengths may be spin relaxation lengths in disguise. Therefore, to unambiguously identify the OAM generation in Cu, a systematic study using an orbital-selective measurement is desired.

In this paper, we investigate OAM accumulation in pristine (non-oxidized) and oxidized Cu through MOKE measurements, which are known to be significantly more sensitive to OAM than to spin in light metals.[27,30] For pristine Cu, we observe a considerable MOKE signal under electric bias. The observed thickness dependence is well described by the phenomenological orbital drift-diffusion model using the effective orbital Hall conductivity obtained from the first-principles calculation. This demonstrates that Cu exhibits significant bulk-originated OHE, contrary to common belief. The extracted orbital diffusion length is 8 nm at room temperature, which is about 50 times smaller than the well-known spin diffusion length of 400 nm in Cu,[31-34] thus confirming that the observed signal is *not* the spin signal in disguise. The estimated orbital diffusivity is two orders of magnitude smaller than the charge diffusivity, indicating that orbital transport can behave significantly differently from charge or spin transport.[35] Next, we examine the Kerr rotation on naturally oxidized Cu films. In contrast to the pristine Cu, a pronounced MOKE signal is observed in films thinner than the light penetration depth, where the bulk OHE is suppressed. Moreover, the signal is nearly independent of the Cu thickness. These observations clearly indicate that the OAM generation in oxidized Cu occurs at the interface, where the OREE dominates.

Results

Sample preparation and MOKE measurement

We fabricated pristine and oxidized Cu films using magnetron sputtering. First, Cu(t_{Cu}) (number in a unit of nm) films were grown, where t_{Cu} varies from 10 to 70 nm. For the pristine Cu

samples, a 5 nm Si_3N_4 capping layer was deposited on top of Cu immediately after the Cu growth without breaking vacuum. For oxidized Cu samples, the deposited Cu film was exposed to ambient air for one hour to allow natural oxidation at the surface. Then, a 5 nm Si_3N_4 capping layer was deposited to prevent further oxidation. All samples were deposited onto sapphire (0001) substrates under the base pressure of $< 1\times10^{-7}$ torr, the operating Ar pressure of 3 mTorr, flow rate of 30 sccm, and temperature of 300 K. The crystal structure of Cu was confirmed by X-ray diffraction (Supplementary Note 1). Our Cu films have polycrystalline structure with (111) texture along the out-of-plane direction. The resistivity (ρ) of Cu was characterized by 4-point probe measurement. A ρ of 2.3 $\mu\Omega$·cm was achieved at the bulk region (thickness 70 nm), then it increased to 15 $\mu\Omega$·cm at a thickness of 10 nm because of the surface scattering[36] (Supplementary Note 1). The complex refractive index ($\tilde{n} = n + ik$) of 0.4+ i4.8 of Cu at the wavelength of 780 nm was obtained by the spectroscopic ellipsometry technique (Supplementary Note 1). To apply an electrical bias, the Cu films were patterned into a 20 μm wide channel structure using standard photolithography and Ar ion milling (Supplementary Note 1).

The current-induced magnetic moment accumulated on the Cu top interface was measured by longitudinal MOKE (Fig. 1c).[37] An electric field applied into the x-direction generates a y-component magnetic polarization, which can originate from various origins, such as the spin/orbital Hall effect (Fig. 1a) or the spin/orbital Rashba-Edelstein effect (Fig. 1b). The s-polarized laser (polarization of light is perpendicular to the plane of incident) with wavelength λ = 780 nm is focused by a lens and incident on the sample with an incidence angle (ϕ) of 25˚. After the light interacts with the accumulated magnetic moment and is reflected, its polarization is rotated, and the Kerr rotation (θ_K) is measured by a balanced detector (Fig. 1c). We used a mechanical relay switch and sapphire substrate to suppress the Joule heating contribution on the MOKE measurement (see Method for details of MOKE measurement).

With an oblique incidence, θ_K has contributions from both the polar and longitudinal components of magnetization. These two sources of θ_K are evident in the channel position dependence measurement of pristine Cu(60) (Fig. 2a). The polar component of θ_K does not depend on the incidence angle of light (ϕ) and shows an asymmetric profile along the channel width, which comes from the Oersted field (shown later). Conversely, the longitudinal component of θ_K critically depends on the incidence angle and shows a symmetric profile. Especially, at the channel

center, where the Oersted-field-driven polar component gets nulled, the measured θ_K is dominated by the longitudinal component and changes its sign with the reversal of the incidence angle (Fig. 2b). The linear dependence on the charge current density (j_c) confirms that the Joule heating effect does not contribute to the MOKE measurement. Taking the odd component, $[\theta_K(\phi>0) - \theta_K(\phi<0)]/2$, we extracted the longitudinal component of the entire channel, which is nearly uniform along the channel width (Fig. 2c).

Determination of magneto-optical constant using polar MOKE

To quantify the magnitude of θ_K, we need to determine the magneto-optical constant (Q) of Cu, i.e., the optical sensitivity to the magnetization induction. Using first-principles calculations for bulk Cu, we evaluate the magneto-optical constants $Q_{spin} = -0.054-0.11i$ (μ_B per atom)$^{-1}$ and $Q_{orbital} = -1.3-0.72i$ (μ_B per atom)$^{-1}$ at the photon energy 1.58 eV, which arise from the induced spin and orbital moments by the Zeeman interaction, respectively (see Supplementary Note 2 for the $Q_{spin/orbital}$ calculation). Thus, we expect that the magneto-optical response in Cu would be dominated by the orbital magnetization, if the induced spin and orbital moments are comparable to each other. Although $Q_{spin/orbital}$ exhibits a dependence on photon energy, $Q_{orbital}$ is consistently larger in magnitude than Q_{spin} throughout the photon energy range of 1~6 eV. However, our theoretical calculations may not give quantitatively accurate values for $Q_{spin/orbital}$, since the magneto-optical response in noble metals may strongly depend on extrinsic parameters.[38] Therefore, in the following, we provide experimental determinations of $Q_{spin/orbital}$ of Cu.

The polar MOKE result, measured at ϕ=0 on pristine Cu follows the profile of the z-component Oersted field (H_{Oe}^{z}). The H_{Oe}^{z}-driven complex polar Kerr angle ($\tilde{\theta}_K^P$) is expressed by

$$\tilde{\theta}_K^P = \left(\tilde{\theta}_K^P\right)_\infty^{spin/orbital} \chi_{spin/orbital} H_{Oe}^{z} = \frac{-inQ_{spin/orbital}}{n^2-1} \chi_{spin/orbital} H_{Oe}^{z}, \quad (1)$$

where $\left(\tilde{\theta}_K^P\right)_\infty^{spin/orbital}$ is the spin/orbital complex polar Kerr angle per unit magnetization in bulk Cu, $\chi_{spin/orbital}$ is the spin/orbital susceptibility of Cu, and $Q_{spin/orbital}$ is the spin/orbital contribution to the linear magneto-optical constant of Cu. Since the photon energy of 1.58 eV is insufficient to excite core electrons, the MOKE is expected to primarily originate from conduction electrons.[38] Therefore, we use χ_{spin} and $\chi_{orbital}$ of Cu for conduction electrons only: χ_{spin} of 1.9×10^{-9} μ_B atom^{-1}

Oe^{-1} and $\chi_{orbital}$ of -2.4×10^{-9} μ_B $atom^{-1}$ Oe^{-1}.[39] Although χ_{spin}, and $\chi_{orbital}$ are comparable in magnitude, $Q_{orbital}$ is much larger than Q_{spin}, as predicted by our first-principles calculations. This is because Q_{spin} relies on the weak spin-orbit coupling in Cu whereas $Q_{orbital}$ does not. Using $\chi_{orbital}$ of -2.4×10^{-9} μ_B $atom^{-1}$ Oe^{-1} and fitting with the experimentally measured $\tilde{\theta}_K^P$, we obtained $Q_{orbital}$ = $(-3.2\pm1.0)-(2.0\pm0.6)i$ (μ_B per atom)$^{-1}$(Fig. 3a and b). Compared with earlier work on Ti, it is an order of magnitude larger than the value of Ti. Such a high $Q_{orbital}$ makes MOKE an ideal tool for investigating the orbital generation mechanism in Cu. On the other hand, Q_{spin} of $-0.016+i0.001$ (μ_B per atom)$^{-1}$ was previously determined from the intense spin accumulation during the ultrafast demagnetization of a FM in a FM/Cu bilayer.[40,41] Inserting this Q_{spin} and χ_{spin} of 1.9×10^{-9} μ_B $atom^{-1}$ Oe^{-1} in Eq. (1), we can calculate $\tilde{\theta}_K^P$ (see Supplementary Note 3 for Oersted-field-induced spin polarization): at the edge of the Cu channel, $\tilde{\theta}_K^P \approx (0.1 + i0)$ nrad for the spin magnetization, which is two hundred times smaller than the measured $\tilde{\theta}_K^P \approx (20 + i15)$ nrad. Therefore, we conclude that the measured $\tilde{\theta}_K^P$ is mostly driven by the orbital magnetization.

Thickness dependence of longitudinal MOKE

Next, we investigated the Cu thickness dependence of the longitudinal component of θ_K (θ_K^L) using the determined $Q_{orbital}$ = $-3.2-2.0i$ (μ_B per atom)$^{-1}$. Ignoring the spin signal, there are two sources of measured θ_K^L: one is *y*-component Oersted field (H_{Oe}^y) and the other is the OHE. We found that at a small incidence angle of 25°, the H_{Oe}^y-driven θ_K^L is ten times smaller than the measured θ_K^L (Supplementary Note 4). Therefore, the measured θ_K^L should be dominated by the orbital accumulation due to OHE. To determine the orbital accumulation profile, we performed Cu thickness (t_{Cu}) dependent θ_K^L and the Kerr ellipticity ε_K^L measurements (Fig. 4). Both θ_K^L and ε_K^L show a gradual increase and saturation behavior with increasing t_{Cu}, and the saturation values are comparable to those for Ti.[27] The complex longitudinal Kerr rotation ($\tilde{\theta}_K^L = \theta_K^L + i\varepsilon_K^L$) due to orbital accumulation as a function of t_{Cu} is given by

$$\tilde{\theta}_K^L(t_{Cu}) = \left(\tilde{\theta}_K^L\right)_\infty^{orbital} \int_0^{t_{Cu}} M_y(z)\kappa e^{-\kappa z} dz, \quad (2)$$

Here, $\left(\tilde{\theta}_K^L\right)_\infty^{orbital}$ is determined from $Q_{orbital}$ as $\left(\tilde{\theta}_K^L\right)_\infty^{orbital} = \frac{\cos\phi_0 \tan\phi_1}{\cos(\phi_0-\phi_1)} \frac{i\tilde{n}Q_{orbital}}{\tilde{n}^2-1}$, where ϕ_0 is the incidence angle of light, ϕ_1 is the refraction angle inside Cu films, and $\tilde{n}$ is the complex refractive

index of Cu. $M_y(z)$ is the *y*-component of the orbital profile along the *z*-position in a Cu film and $\kappa = \frac{-4\pi i\tilde{n}cos\phi_1}{\lambda}$ describes a light penetration effect,[37] where λ is the wavelength of light.

For the pristine Cu film, the MOKE response is suppressed at a thin thickness limit, and it gradually increases and then saturates with the Cu thickness. We analyzed that the thickness dependence of orbital edge accumulation is a result of competition between the OHE-driven orbital generation and scattering-driven orbital relaxation. The orbital accumulation $M_y(z)$ in the presence of the OHE is obtained by employing the drift-diffusion equation (see Supplementary Note 5):

$$M_y(z) = M_0 \frac{\sinh[(\frac{t_{\mathrm{Cu}}}{2} - z)/l_{\mathrm{L}}]}{\cosh(t_{\mathrm{Cu}}/2l_{\mathrm{L}})}, \quad (3)$$

where $M_0 = \gamma_{\mathrm{L}}\sigma_{\mathrm{OH}}^{\mathrm{eff}}\tau_{\mathrm{L}}j_c\rho/l_L$, γ_{L} is the gyromagnetic ratio for orbital, $\sigma_{\mathrm{OH}}^{\mathrm{eff}}$ is the effective orbital Hall conductivity, l_{L} is the orbital relaxation length, and τ_{L} is the orbital relaxation time. Firstly, l_{L}=8±3 nm was determined from the relative change of the MOKE signal with the Cu thickness (see Supplementary Note 6 for fits performed with different l_{L} values). Then, M_0=(0.14±0.04)×10^{-5} μ_{B} per atom (at j_c=10^7 A cm^{-2}) was determined from the saturated Kerr rotation at the thick thickness limit. Note that the effective orbital Hall conductivity is used instead of the conventional orbital Hall conductivity to better account for the intrinsic orbital relaxation due to the crystal field.[27] From first-principles calculations for a Cu film (see Supplementary Note 7 for $\sigma_{\mathrm{OH/SH}}^{\mathrm{eff}}$ calculation), we obtain $\sigma_{\mathrm{OH}}^{\mathrm{eff}}$ of 1000 ($\hbar/e$)(Ω·cm)$^{-1}$ and the effective spin Hall conductivity ($\sigma_{\mathrm{SH}}^{\mathrm{eff}}$) of 50 ($\hbar/e$)(Ω·cm)$^{-1}$, which better accounts for the intrinsic spin relaxation due to spin-orbit coupling. Note that $\sigma_{\mathrm{OH}}^{\mathrm{eff}}$ is much larger than $\sigma_{\mathrm{SH}}^{\mathrm{eff}}$, implying a considerable orbital accumulation, as opposed to a negligible spin accumulation. Although our calculation assumes a single crystalline structure, the orbital Hall conductivity is not expected to vary significantly in a polycrystalline structure (Supplementary Note 8). This result, together with a significant disparity between the values of $\left(\tilde{\theta}_{\mathrm{K}}^{\mathrm{L}}\right)_{\infty}^{\mathrm{orbital}}$ and $\left(\tilde{\theta}_{\mathrm{K}}^{\mathrm{L}}\right)_{\infty}^{\mathrm{spin}}$, enables us to disregard the Kerr angle due to the spin Hall effect in Cu.

In this fitting, we considered a weak background (black and blue dashed lines in Fig. 4) that is from H_{Oe}^{y} induced $\tilde{\theta}_{\mathrm{K}}^{\mathrm{L}}$. Nonetheless, the H_{Oe}^{y}-driven $\tilde{\theta}_{\mathrm{K}}^{\mathrm{L}}$ is about ten times smaller than the OHE-driven $\tilde{\theta}_{\mathrm{K}}^{\mathrm{L}}$, so that its effect on the determination of M_0 and l_{L} is not significant. When t_{Cu} is smaller

than optical penetration depth, multiple reflections from Si_3N_4 layer and Sapphire substrate affect the fitting results. To account for this, we adopted an optical model that treats the entire Air/Si_3N_4/Cu stack (Supplementary Note 9). The fitting results in overlap with those obtained from simpler model that neglects multiple reflections. Therefore, the multilayer reflection does not affect our conclusions.

In the bulk limit, the sign of the MOKE signal arising from the OHE is determined by two main factors [see Eq. (2)]: (i) the bulk MOKE signal per unit orbital moment, and (ii) orbital accumulation, which is in turn determined by the (effective) orbital Hall conductivity. In addition, we note that the sign convention for MOKE signals can differ between studies, so determining the sign of orbital accumulation requires a careful comparison. In our case, for Cu, we followed the sign convention used in Ti.[27] Our theoretical calculations indicate a negative $\left(\theta_{\mathrm{K}}^{\mathrm{L}}\right)_{\infty}^{\mathrm{orbital}}$ and positive σ_{OH}, giving rise to a negative net Kerr rotation (same as Ti), consistent with our experimental observations.

The surface roughness can affect the interface scattering, thus orbital accumulation. The measured roughness remained nearly constant (~1 nm) across all thicknesses (Supplementary Note 10). Therefore, we expect that the roughness might affect the saturation value of orbital accumulation, but it does not affect the thickness dependence.

Impact of surface oxidation

Next, we investigated the surface oxidation effect of Cu. The surface oxidation was achieved by exposing Cu films to an ambient air for one hour. X-ray photoemission spectroscopy (XPS) analysis confirmed that the oxidized surface is composed of Cu_2O and this oxidation state exists uniformly for films with different Cu thicknesses (Supplementary Note 11). The chemical analysis indicated that a 2 nm-thick CuO_x layer exists on top of the unoxidized Cu film (Supplementary Note 12). The surface oxidation effect on the orbital generation was revealed by longitudinal MOKE measurements of the 10 nm-thick Cu film (Fig. 5), where the bulk OHE is minimized (Fig. 4). The partially oxidized Cu film shows a significant $\theta_{\mathrm{K}}^{\mathrm{L}}$ of 18 nrad at $j_c=10^7$ A cm^{-2}, which is significantly larger than $\theta_{\mathrm{K}}^{\mathrm{L}}$ of 3 nrad for the unoxidized 10 nm-thick Cu film (Fig. 4). Interestingly, $\theta_{\mathrm{K}}^{\mathrm{L}}$ of the partially oxidized Cu films is nearly independent of the Cu thickness, see Fig. 5e, which indicates the interfacial origin of the orbital generation. The OREE-driven OAM at the interface

can diffuse to unoxidized part of Cu as $M_y(z) = M_0 \exp(-z/l_{\mathrm{L}})$, where z=0 is the interface position, M_0 describes the OREE efficiency, and l_L=8 nm is determined above (see Supplementary Note 9 for Kerr angle calculation and fits incorporating multilayer reflections). Together with Eq. (2), we obtain the saturation behavior of $\theta_{\mathrm{K}}^{\mathrm{L}}$ after the Cu thickness of 8 nm (fittings in Fig. 5e). However, the realistic thickness-dependence would be more complicated because the charge current density at the interfacial region will be different from thickness-averaged current density. We note that, at the thick limit of 60 nm, $\theta_{\mathrm{K}}^{\mathrm{L}}$ of the oxidized Cu is close to that of the pristine Cu. We speculate that, with a thick Cu thickness, charge current mostly flows in the unoxidied part of Cu and OHE becomes dominant. On the other hand, with a thin Cu thickness, a significant portion of charge current flows near the CuO_x interface and OREE becomes dominant. Assuming that the OHE contribution does not change with the existence of the interfacial oxide, we distinguished OREE and OHE contributions in Fig. 5e.

Although the substrate/Cu interface can contribute to OREE in principle, we regard substrate effect as unlikely for two reasons. First, sputtered Cu atoms land with insufficient energy to break the bonds of an insulating substrate, so no chemical reaction occurs at the bottom interface.[42] Second, the thickness dependence of the Kerr angle does not match the signature expected from an OREE at the substrate/Cu interface. As previously described, OREE at the substrate is expressed as $M_y(z) = M_0 \exp[(z - t_{\mathrm{Cu}})/l_{\mathrm{L}}]$. It would generate a large Kerr rotation in thin Cu that decays to zero once t_{Cu} far exceeds the optical penetration depth combined with l_{L}. Instead, our pristine Cu data rise with thickness and then saturate, and oxidized Cu shows monotonic saturation behavior (see Supplementary Note 13 for fits based on the substrate-Cu interface OREE). We also ignore the Cu/Si_3N_4 interface contribution to OREE based on the lack of MOKE response in thin limit (10 nm) of pristine Cu.

Discussion

For pristine Cu, the relation $M_0 = \gamma_{\mathrm{L}} \sigma_{\mathrm{OH}}^{\mathrm{eff}} \tau_{\mathrm{L}} j_{\mathrm{c}} \rho / l_L$, using the fitted parameters M_0 and l_{L}, yields the orbital relaxation time τ_{L} of 0.65±0.35 ps. This value is very close to τ_{L}=0.35±0.1 ps, recently reported in a time-resolved THz emission experiment on Ni/Cu.[22] Meanwhile, the relaxation time is related to the orbital diffusivity D_{L} through the relation $l_{\mathrm{L}}^2 = D_{\mathrm{L}} \tau_{\mathrm{L}}$, which leads to D_{L} of 100 nm^2 ps^{-1}. In many previous studies, D_{L} has been assumed to be the same as the charge diffusivity D_{c}.

For Cu, D_c is determined to be 10,000 nm^2 ps^{-1} from $D_c = (1/e^2\rho N_F)$, where N_F is the density of states at the Fermi level. Note that D_L is two orders of magnitude smaller than D_c, which is in stark contrast to the spin diffusivity D_S, which is assumed to be the same as D_c in many materials. This implies that orbital transport is significantly different from spin transport in its nature. We attribute the much smaller D_L to strong crystal field that transfers OAM to the lattice[43].

A few previous studies have reported D_S or D_L values smaller than D_c. First, Vélez et al.[44] reported smaller D_S than D_c in Pt. Like Pt, materials with strong spin-orbit coupling show both the spin Hall effect and OHE[4,5,7]. Therefore, distinguishing spin or orbital contributions are challenging. Second, Sala *et al.* reported D_L is smaller than D_c in Mn, which has weak spin-orbit coupling. In their work, D_L was 2.5 nm^2 ps^{-1}. Using a Mn resistivity ρ = 2.3 $\mu\Omega$·m, $D_c = (1/e^2\rho N_F)$ is determined to be 6 nm^2 ps^{-1}, so $D_c/D_L \approx 2$. Our prediction of $D_c/D_L \approx 100$ suggests a much stronger suppression of orbital diffusion in Cu.

Several calculations[23-25,45] reported a very short orbital diffusion length of a few atomic spacings for various transition metals including Pt,[23,25,45] Cu,[23] Cr,[23] and V.[23] This value is one to two orders of magnitude smaller than experimentally determined values for Cr,[26] Ti,[27-29] and Pt.[46] It was suggested[23] that experiments may have measured the spin diffusion length l_S instead of l_L. However, the known l_S of 400 nm of Cu is fifty-times larger[31-34] than our determination of l_L of 8 nm. Note that other reports from the THz emission measurement[22], the torque measurement[14,16], and the nonlocal electrical measurement have reported l_L of 6–100 nm of Cu.[47] Further research for orbital transport, including electron-phonon interaction and polycrystallinity effect,[29,48] is required to bridge the gap between theory and experiment.

Recently, a theory proposed an alternative mechanism for orbital accumulation, driven by the transverse gradient of the longitudinal response (i.e., the vorticity of the electron flow) rather than by the orbital Hall effect.[49] In this case, the orbital accumulation profile is determined by mean free path rather than by the orbital diffusion length. However, we estimate that the magnitude of the vorticity-driven orbital accumulation is an order of magnitude smaller than the value obtained from our analysis based on the OHE. Further research is hence required to examine the proposed vorticity-driven effect (Supplementary Note 14).

Conclusion

Owing to the high conductivity and long spin diffusion length, Cu has been widely used for various electronics and spintronics applications. Recent discoveries of the current-generated orbital physics, through the OHE and OREE, suggest that Cu can play an important role in orbitronics as well. Using MOKE microscopy, we directly measured OHE-driven orbital accumulation in pristine Cu and OREE-driven orbital accumulation in oxidized Cu. From the thickness profile of the orbital accumulation, we determined the orbital diffusion length of 8±3 nm, which is 50 times smaller than the spin diffusion length of 400 nm.[31-34] The short orbital diffusion length indicates that the scattering mechanism and dissipation for orbital angular moment are significantly different from that for spin. The magnitude of the orbital accumulation is explained by the orbital Hall conductivity of 1000 $(\hbar/e)(\Omega\cdot\mathrm{cm})^{-1}$ and the orbital relaxation time of 0.65 ps. The relationship between the orbital relaxation time and the orbital diffusion length suggests that orbital diffusivity is two orders of magnitude smaller than the charge diffusivity, which starkly contrasts the spin diffusivity being comparable to the charge diffusivity in many materials. This discrepancy indicates that the orbital transport may be qualitatively different from the spin transport.

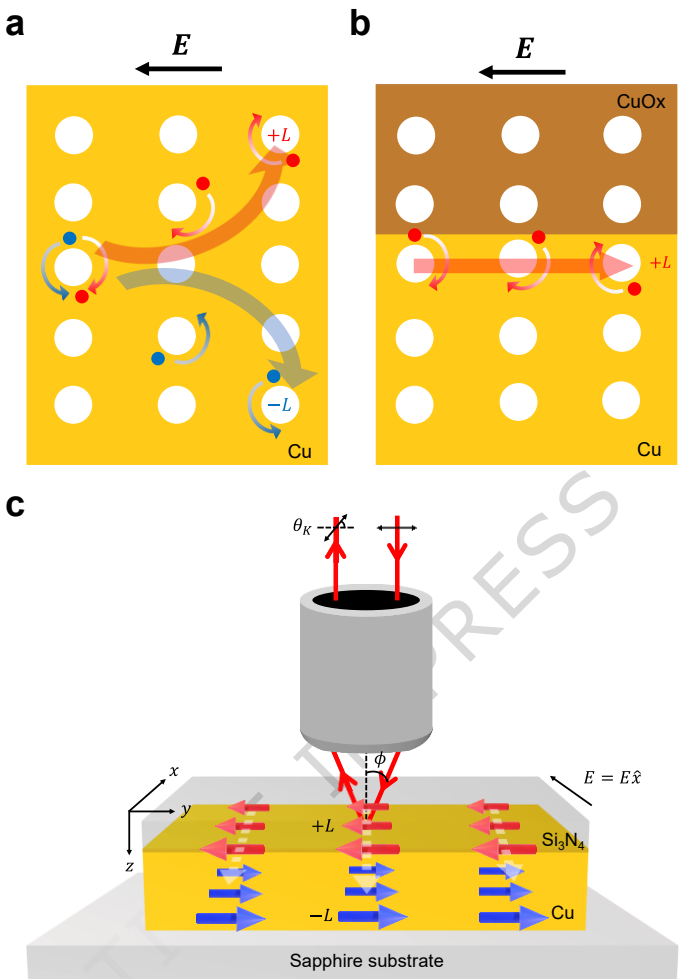

Fig. 1. Schematics of experiment. a Orbital Hall effect in a centrosymmetric system. When an electric field (***E***) is applied to pristine Cu, electrons with positive and negative orbital angular momentum ($+L$ and $-L$) move upward and downward, respectively (red and blue circles), and an orbital current is generated transverse to ***E***. **b** Orbital Rashba-Edelstein effect in an inversion-symmetry broken system. When ***E*** is applied to oxidized Cu, electrons with $+L$ are generated locally at the inversion-symmetry broken region. Orbital moment is generated at the interface between Cu and CuO_x. **c** Longitudinal magneto-optical Kerr effect experiment. When ***E*** is applied in the x direction of the device, orbital moments with opposite angular momentum ($+L$ and $-L$) accumulate at the top and bottom surface. Linearly polarized light with incidence angle ϕ interacts with y component of orbital angular momentum and is reflected with Kerr angle (θ_K).

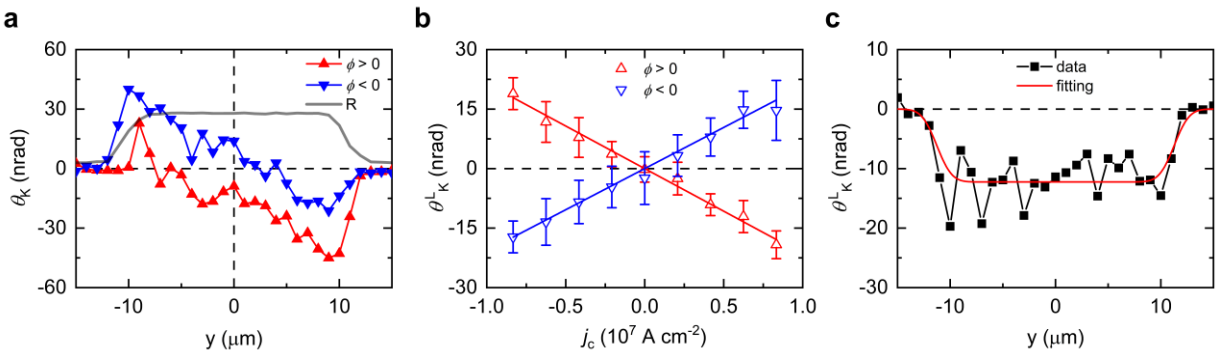

Fig. 2. Magneto-optical Kerr effect (MOKE) measurement on pristine Cu. a Spatial position (y) dependence of longitudinal MOKE measurement (ϕ=±25˚) on pristine Cu(60). Red upward and blue downward triangles are experimental data for ϕ=+25˚ and ϕ=-25˚, respectively. Grey solid lines are reflectivity data expressed in arbitrary unit. **b** Dependence of θ_K^L on the current density (j_c) measured at the center of the channel (y=0). Red upward and blue downward triangles are experimental data for ϕ=+25˚ and ϕ=-25˚, respectively. Red and blue solid lines are linear regression fits of the experimental data. The error bars indicate standard deviation of repeated measurements. **c** Longitudinal MOKE signal from spatial position dependence measurement. Black square is the data taken from the odd component of θ_K^L in (a), $[\theta_K(\phi>0) - \theta_K(\phi<0)]/2$. Red solid line is the fitting curve which is uniform along the channel width.

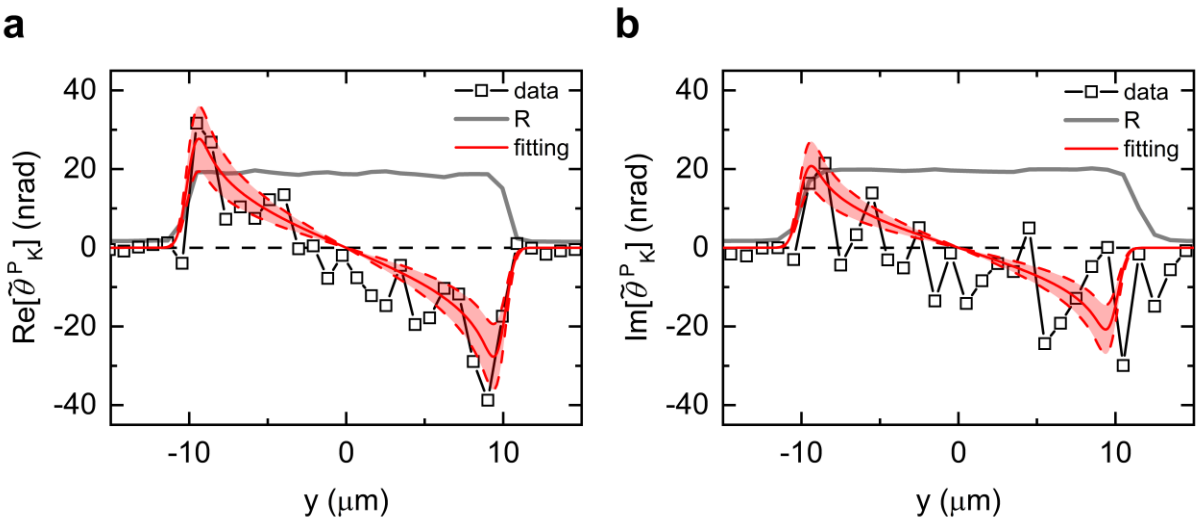

Fig. 3. Determination of the magneto-optical constant. **a,b** Spatial position dependence of polar magneto-optical Kerr effect measurement (ϕ=0˚) for **a** real and **b** imaginary part of the complex Kerr angle (Re$\left[\tilde{\theta}^{\mathrm{P}}_{\mathrm{K}}\right]$ and Im$\left[\tilde{\theta}^{\mathrm{P}}_{\mathrm{K}}\right]$). Black squares are experimental data, and red solid lines are fits with the calculated Oersted field based on orbital magnetization. The red shaded area indicates the uncertainty range corresponding to a ±30% variation in the Q_{orbital} of $-3.2-2.0i$ (μ_{B} per atom)$^{-1}$. Grey solid lines are reflectivity (R) data expressed in arbitrary unit.

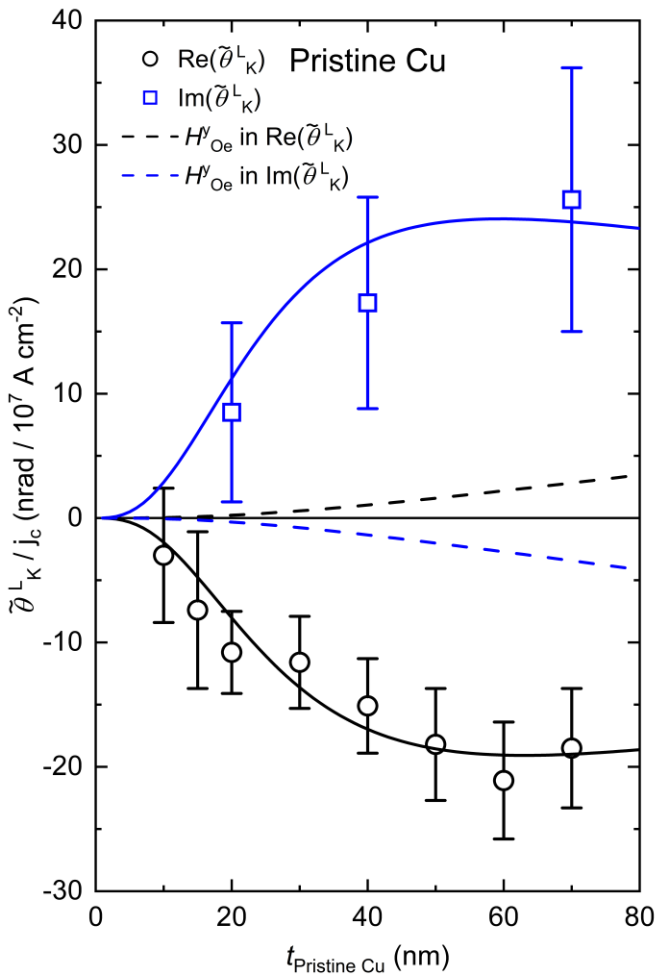

Fig. 4. Cu thickness dependence of longitudinal magneto-optical Kerr effect measurements. Black circles and blue squares are real and imaginary Kerr angle normalized by current density (j_c) ($\mathrm{Re}[\tilde{\theta}^L_K]/j_c$ and $\mathrm{Im}[\tilde{\theta}^L_K]/j_c$). The error bars indicate standard deviation of repeated measurements. Black and blue solid lines are fits based on the theoretical calculation of the orbital Hall effect with M_0=(0.14±0.04)×10^{-5} μ_B per atom per j_c=10^7 A cm^{-2} and l_L=8±3 nm. Black and blue dashed lines represent $\mathrm{Re}[\tilde{\theta}^L_K]/j_c$ and $\mathrm{Im}[\tilde{\theta}^L_K]/j_c$ induced by the Oersted field (H^y_{Oe}), respectively.

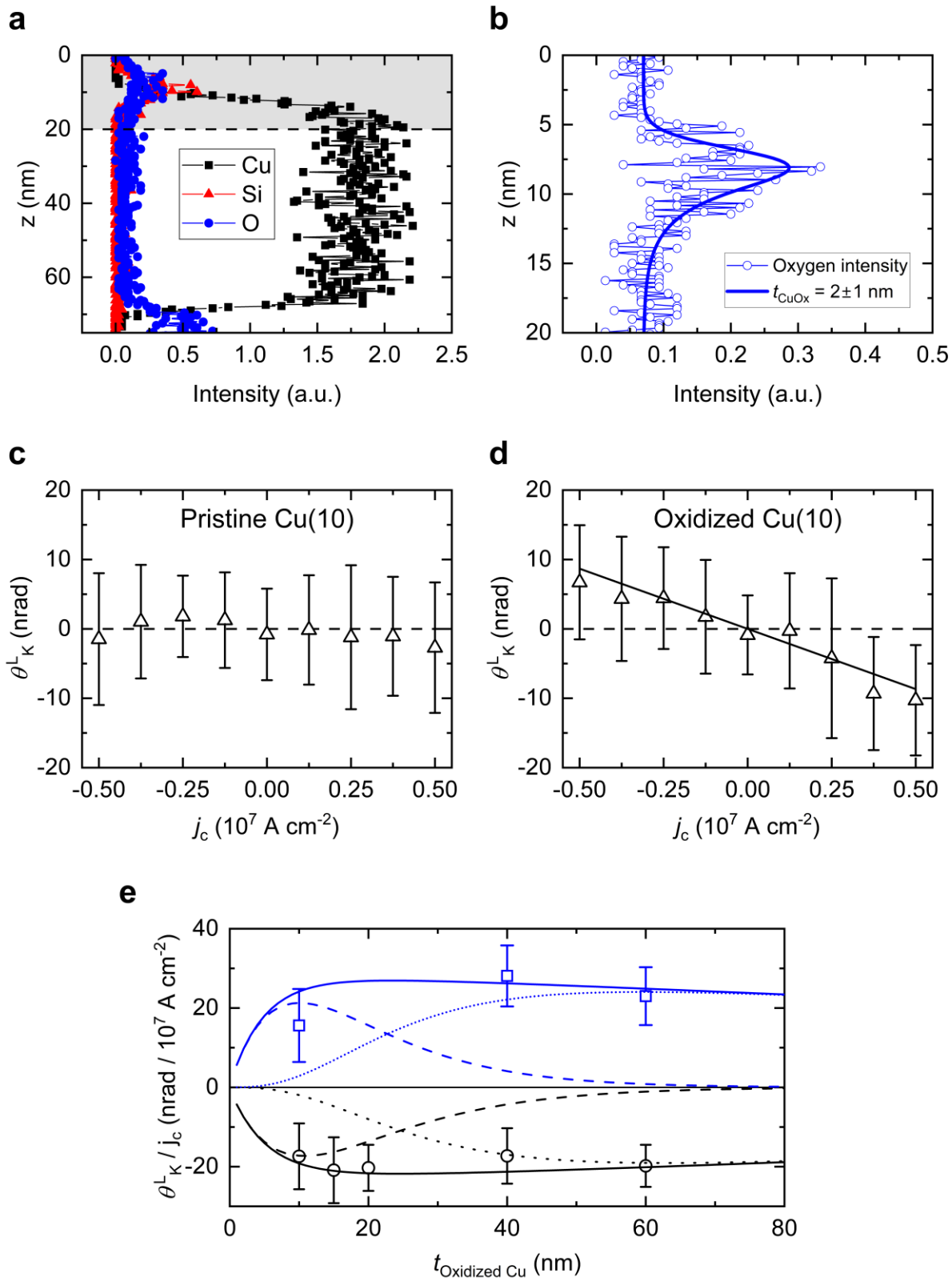
a
z (nm)
Intensity (a.u.)
Cu
Si
O
b
z (nm)
Intensity (a.u.)
Oxygen intensity
t_{CuOx} = 2±1 nm
c
Pristine Cu(10)
θ^L_K (nrad)
j_c (10^7 A cm^{-2})
d
Oxidized Cu(10)
θ^L_K (nrad)
j_c (10^7 A cm^{-2})
e
θ^L_K / j_c (nrad / 10^7 A cm^{-2})
$t_{Oxidized\ Cu}$ (nm)

Fig. 5. Magneto-optical Kerr effect (MOKE) measurement on oxidized Cu. a Elemental intensity profiles of Cu (black squares), Si (red triangles), and O (blue circles) extracted from the energy dispersive spectroscopy (EDS) line mapping. **b** EDS line spectrum of oxygen in the sample. The oxidized Cu (CuO_x) layer, with a thickness of 2±1 nm, exists on top of the unoxidized Cu film. **c,d** Dependence of θ_K^L on the current density (j_c) measured on the **c** pristine Cu(10 nm) and **d** oxidized Cu(10 nm) film. The black upward triangles are experimental data for ϕ=+25˚, and the black solid line is the linear regression fit of experimental data. **e** Dependence of the longitudinal MOKE measurement on the Cu thickness (t_{Cu}), which is the total thickness of the oxidized and unoxidized Cu. Black circles and blue squares are real and imaginary Kerr angle normalized by current density (j_c). The error bars indicate standard deviation of repeated measurements. Solid lines are fits using equation (2). The orbital accumulation is assumed as $M_y(z) = M_0 \exp(-z/l_L)$, where M_0 = 0.14×10^{-5} μ_B per atom at j_c = 10^7 A cm^{-2} and l_L = 8 nm. Dotted lines are the orbital Hall effect contribution, assumed to be unaffected by surface oxidation, and dashed lines are the orbital Rashba-Edelstein contribution after subtracting the orbital Hall effect component.

Methods

MOKE measurement

A pulsed laser emitting at 780 nm (Coherent, Chameleon Vision-S) served as the light source. After passing through an initial polarizer the beam was prepared in s-polarization. It passed a non-polarizing beam splitter and was routed into a 50x objective lens (Mitutoyo Plan Apo, NA=0.75), which focused ≈ 1 μm spot on the sample.

For polar MOKE the beam was incident normal to the sample, whereas for longitudinal MOKE the objective was laterally offset so that the beam entered the edge of its pupil, producing an incidence angle of 25˚. The reflected light passed back through the beam splitter, a half-wave plate, and a Wollaston prism before reaching a balanced photodetector (Thorlabs, PDB450A-AC). The half-wave plate was adjusted so that the output of balanced photodetector was nulled when the sample magnetization was zero. An ac current at 3017 Hz (Keithley 6221) was driven through the device. The signal of balanced photodetector was demodulated with a lock-in amplifier (Stanford Research Systems, SR830). Data were acquired using a time constant of 1 s and a low-pass filter slope of 12 dB/octave. The lock-in output was read out every 100 ms. During acquisition, the applied current polarity was alternated using a relay switch (10 s positive, 10 s negative). For each polarity-switching cycle, the measured value was defined as the difference between the mean lock-

in outputs obtained for the two polarities. Each data point represents the average of these cycles accumulated over 30–60 min.

Spatially resolved measurements were obtained by translating the sample with motorized stages while the probe beam remained stationary. To suppress Joule-heating artefacts, a mechanical relay switch swapped the source and drain leads. Signals recorded for the two current polarities were subtracted, isolating only the component that reverses sign with current.

Data availability

The datasets generated and analyzed during the current study are available in the Figshare repository, [10.6084/m9.figshare.28184159].

References

1. Go D, Jo D, Lee H-W, Kläui M, Mokrousov Y. Orbitronics: Orbital currents in solids. *Europhysics Letters* **135**, 37001 (2021).

2. Jo D, Go D, Choi G-M, Lee H-W. Spintronics meets orbitronics: Emergence of orbital angular momentum in solids. *npj Spintronics* **2**, 19 (2024).

3. Burgos Atencia R, Agarwal A, Culcer D. Orbital angular momentum of Bloch electrons: equilibrium formulation, magneto-electric phenomena, and the orbital Hall effect. *Advances in Physics: X* **9**, 2371972 (2024).

4. Tanaka T*, et al.* Intrinsic spin Hall effect and orbital Hall effect in 4 d and 5 d transition metals. *Physical Review B—Condensed Matter and Materials Physics* **77**, 165117 (2008).

5. Kontani H, Tanaka T, Hirashima D, Yamada K, Inoue J. Giant orbital Hall effect in transition metals: Origin of large spin and anomalous Hall effects. *Physical review letters* **102**, 016601 (2009).

6. Go D, Jo D, Kim C, Lee H-W. Intrinsic spin and orbital Hall effects from orbital texture. *Physical review letters* **121**, 086602 (2018).

7. Jo D, Go D, Lee H-W. Gigantic intrinsic orbital Hall effects in weakly spin-orbit coupled metals. *Physical Review B* **98**, 214405 (2018).

8. Salemi L, Berritta M, Nandy AK, Oppeneer PM. Orbitally dominated Rashba-Edelstein effect in noncentrosymmetric antiferromagnets. *Nature communications* **10**, 5381 (2019).

9. Go D, Lee H-W. Orbital torque: Torque generation by orbital current injection. *Physical review research* **2**, 013177 (2020).

10. An H, Kageyama Y, Kanno Y, Enishi N, Ando K. Spin–torque generator engineered by natural oxidation of Cu. *Nature communications* **7**, 13069 (2016).

11. Okano G, Matsuo M, Ohnuma Y, Maekawa S, Nozaki Y. Nonreciprocal spin current generation in surface-oxidized copper films. *Physical review letters* **122**, 217701 (2019).

12. Tazaki Y*, et al.* Current-induced torque originating from orbital current. *arXiv preprint arXiv:200409165*, (2020).

13. Ding S*, et al.* Harnessing orbital-to-spin conversion of interfacial orbital currents for efficient spin-orbit torques. *Physical review letters* **125**, 177201 (2020).

14. Kim J*, et al.* Nontrivial torque generation by orbital angular momentum injection in ferromagnetic-metal/Cu/Al 2 O 3 trilayers. *Physical Review B* **103**, L020407 (2021).

15. Ding S*, et al.* Observation of the orbital Rashba-Edelstein magnetoresistance. *Physical review letters* **128**, 067201 (2022).

16. Kim J*, et al.* Oxide layer dependent orbital torque efficiency in ferromagnet/Cu/oxide heterostructures. *Physical review materials* **7**, L111401 (2023).

17. Ding S, Kang M-G, Legrand W, Gambardella P. Orbital torque in rare-earth transition-metal ferrimagnets. *Physical Review Letters* **132**, 236702 (2024).

18. Santos E, Abrão J, Vieira A, Mendes J, Rodríguez-Suárez R, Azevedo A. Exploring orbital-charge conversion mediated by interfaces with Cu O x through spin-orbital pumping. *Physical Review B* **109**, 014420 (2024).

19. Mendoza-Rodarte J, Cosset-Chéneau M, Van Wees B, Guimarães M. Efficient magnon injection and detection via the orbital rashba-edelstein effect. *Physical Review Letters* **132**, 226704 (2024).

20. Go D*, et al.* Orbital Rashba effect in a surface-oxidized Cu film. *Physical Review B* **103**,

L121113 (2021).

21. Liu Q, Zhu L. Absence of orbital current torque in Ta/ferromagnet bilayers. *Nature Communications* **16**, 8660 (2025).

22. Xu Y*, et al.* Orbitronics: light-induced orbital currents in Ni studied by terahertz emission experiments. *Nature Communications* **15**, 2043 (2024).

23. Rang M, Kelly PJ. Orbital relaxation length from first-principles scattering calculations. *Physical Review B* **109**, 214427 (2024).

24. Urazhdin S. Symmetry constraints on orbital transport in solids. *Physical Review B* **108**, L180404 (2023).

25. Salemi L, Oppeneer PM. First-principles theory of intrinsic spin and orbital Hall and Nernst effects in metallic monoatomic crystals. *Physical Review Materials* **6**, 095001 (2022).

26. Lee S*, et al.* Efficient conversion of orbital Hall current to spin current for spin-orbit torque switching. *Communications Physics* **4**, 234 (2021).

27. Choi Y-G*, et al.* Observation of the orbital Hall effect in a light metal Ti. *Nature* **619**, 52-56 (2023).

28. Hayashi H*, et al.* Observation of long-range orbital transport and giant orbital torque. *Communications Physics* **6**, 32 (2023).

29. Idrobo JC*, et al.* Direct observation of nanometer-scale orbital angular momentum accumulation. *arXiv preprint arXiv:240309269*, (2024).

30. Lyalin I, Alikhah S, Berritta M, Oppeneer PM, Kawakami RK. Magneto-optical detection of the orbital Hall effect in chromium. *Physical Review Letters* **131**, 156702 (2023).

31. Jedema FJ, Filip A, Van Wees B. Electrical spin injection and accumulation at room temperature in an all-metal mesoscopic spin valve. *Nature* **410**, 345-348 (2001).

32. Jedema F, Nijboer M, Filip A, Van Wees B. Spin injection and spin accumulation in all-metal mesoscopic spin valves. *Physical Review B* **67**, 085319 (2003).

33. Kimura T, Hamrle J, Otani Y. Estimation of spin-diffusion length from the magnitude of

spin-current absorption: Multiterminal ferromagnetic/nonferromagnetic hybrid structures. *Physical Review B—Condensed Matter and Materials Physics* **72**, 014461 (2005).

34. Kimura T, Sato T, Otani Y. Temperature evolution of spin relaxation in a NiFe/Cu lateral spin valve. *Physical review letters* **100**, 066602 (2008).

35. Han S, Lee H-W, Kim K-W. Orbital dynamics in centrosymmetric systems. *Physical review letters* **128**, 176601 (2022).

36. Sondheimer EH. The mean free path of electrons in metals. *Advances in physics* **50**, 499-537 (2001).

37. Stamm C*, et al.* Magneto-optical detection of the spin Hall effect in Pt and W thin films. *Physical review letters* **119**, 087203 (2017).

38. Uba L, Uba S, Antonov V. Magneto-optical Kerr spectroscopy of noble metals. *Physical Review B* **96**, 235132 (2017).

39. d'Avezac M, Marzari N, Mauri F. Spin and orbital magnetic response in metals: susceptibility and NMR shifts. *Physical Review B—Condensed Matter and Materials Physics* **76**, 165122 (2007).

40. Choi G-M, Cahill DG. Kerr rotation in Cu, Ag, and Au driven by spin accumulation and spin-orbit coupling. *Physical Review B* **90**, 214432 (2014).

41. Choi G-M. Magneto-optical Kerr effect driven by spin accumulation on Cu, Au, and Pt. *Applied Sciences* **8**, 1378 (2018).

42. Lim JD, Lee PM, Chen Z. Understanding the bonding mechanisms of directly sputtered copper thin film on an alumina substrate. *Thin Solid Films* **634**, 6-14 (2017).

43. Ning X, Pezo A, Kim K-W, Zhao W, Lee K-J, Manchon A. Orbital Diffusion, Polarization, and Swapping in Centrosymmetric Metals. *Physical Review Letters* **134**, 026303 (2025).

44. Vélez S*, et al.* Hanle magnetoresistance in thin metal films with strong spin-orbit coupling. *Physical review letters* **116**, 016603 (2016).

45. Belashchenko KD*, et al.* Breakdown of the drift-diffusion model for transverse spin transport in a disordered Pt film. *Physical Review B* **108**, 144433 (2023).

46. Moriya H*, et al.* Observation of long-range current-induced torque in Ni/Pt bilayers. *Nano Letters* **24**, 6459-6464 (2024).

47. Gao W*, et al.* Nonlocal electrical detection of reciprocal orbital Edelstein effect. *Nature Communications* **16**, 6380 (2025).

48. Liao L*, et al.* Efficient orbital torque in polycrystalline ferromagnetic-metal/Ru/Al 2 O 3 stacks: Theory and experiment. *Physical Review B* **105**, 104434 (2022).

49. Valet T, Jaffres H, Cros V, Raimondi R. Quantum Kinetic Anatomy of Electron Angular Momenta Edge Accumulation. *arXiv preprint arXiv:250706771*, (2025).

Acknowledgements

KHK and GMC were financially supported by the National Research Foundation (NRF) grant funded by Korea government (RS-2025-00519398, RS-2024-00410027). DJ and PMO were financially supported by the Swedish Research Council (VR), the Knut and Alice Wallenberg Foundation (Grants No. 2022.0079 and 2023.0336), and by the Wallenberg Initiative Materials Science for Sustainability (WISE) funded by the Knut and Allice Wallenberg Foundation. This work was further supported by the EIC Pathfinder OPEN grant 101129641 ″OBELIX”. The calculations were enabled by resources provided by the National Academic Infrastructure for Supercomputing in Sweden (NAISS) at NSC Linköping, partially funded by VR through Grant Agreement No. 2022-06725. HWL was financially supported by the Samsung Science and Technology Foundation (Grant No. BA-1501-51) and the National Research Foundation of Korea (NRF) (No. RS-2024-00410027).

Author contributions

KHK fabricated samples and performed MOKE measurements with the help of GMC. DJ performed the theoretical calculation with the help of HWL and PMO. All authors wrote the manuscript.

Competing interests

The authors declare no competing interests.

Additional information

Supplementary information

The online version contains supplementary material available at ~.

Editor Summary-

The electrical generation of orbital angular momentum in materials has attracted significant attention due to its fundamental importance and technological potential. Here, the authors demonstrate current-induced orbital accumulation in pristine and naturally oxidized Cu films using magneto-optical Kerr effect measurements.

Peer Review Information-

Communications Physics thanks Delin Zhang and the other, anonymous, reviewer(s) for their contribution to the peer review of this work. A peer review file is available.